

1 **Smooth crustal velocity models cause a depletion of high-frequency ground**  
2 **motions on soil in 2-D dynamic rupture simulations**

3  
4 **Yihe Huang<sup>1</sup>**

5 <sup>1</sup>Department of Earth and Environmental Sciences, University of Michigan.

6 Corresponding author: Yihe Huang ([yiheh@umich.edu](mailto:yiheh@umich.edu))

7  
8 This paper is a preprint submitted to EarthArXiv. It is under review in the Bulletin of the  
9 Seismological Society of American (BSSA). Please feel free to contact the author if you have  
10 any feedback.  
11  
12  
13  
14  
15  
16  
17  
18  
19  
20  
21  
22  
23  
24  
25  
26  
27  
28  
29  
30  
31

32 **Abstract**

33

34 A depletion of high-frequency ground motions on soil sites has been observed in recent large  
35 earthquakes and is often attributed to the nonlinear soil response. Here we show that the reduced  
36 amplitudes of high-frequency horizontal-to-vertical spectral ratios on soil can also be caused by a  
37 smooth crustal velocity model with low shear wave velocities underneath soil sites. We calculate  
38 near-fault ground motions using both 2-D dynamic rupture simulations and point-source models  
39 for both rock and soil sites. The 1-D velocity models used in the simulations are derived from  
40 empirical relationships between seismic wave velocities and depths in northern California. The  
41 simulations for soil sites feature lower shear wave velocities and thus larger Poisson's ratios at  
42 shallow depths than those for rock sites. The lower shear wave velocities cause slower shallow  
43 rupture and smaller shallow slip, but both soil and rock simulations have similar rupture speeds  
44 and slip for the rest of the fault. However, the simulated near-fault ground motions on soil and  
45 rock sites have distinct features. Compared to ground motions on rock, horizontal ground  
46 acceleration on soil is only amplified at low frequencies, whereas vertical ground acceleration is  
47 deamplified for the whole frequency range. Thus, the horizontal-to-vertical spectral ratios on soil  
48 exhibit a depletion of high-frequency energy. The comparison between smooth and layered  
49 velocity models demonstrates that the smoothness of the velocity model plays a critical role in  
50 the contrasting behaviors of horizontal-to-vertical spectral ratios on soil and rock for different  
51 rupture styles and velocity profiles. Our results reveal the significant role of shallow crustal  
52 velocity structure in the generation of high-frequency ground motions on soil sites.

53

54

55

56

57

58

59

60

61

62

## 63 Introduction

64

65 It is well known that near-surface site effects significantly contribute to strong ground motions  
66 from earthquakes. In particular, sedimentary basins or soil sites are common in seismically active  
67 regions and are often considered to amplify ground motions due to seismic wave reverberations.  
68 However, especially for large earthquakes, the amplification of ground motions seems to  
69 strongly depend on wave frequencies. For example, in the 2019  $M_W$  7.1 Ridgecrest earthquake,  
70 the amplitudes of horizontal-to-vertical spectral ratios (HVSRs) at deep alluvium sites are much  
71 lower than those at thin alluvium and rock sites for frequencies higher than 3 Hz (Hough et al.,  
72 2020). A similar depletion of high-frequency energy on soil sites has been shown for the 1985  
73  $M_W$  8.0 Michoacan, Mexico earthquake, 1989  $M_W$  6.9 Loma Prieta, California earthquake  
74 (Beresnev and Wen, 1996), 1994  $M_W$  6.7 Northridge, California earthquake (Field et al., 1997),  
75 the 2015  $M_W$  7.8 Gorkha, Nepal, earthquake (Dixit et al., 2015), and the 2016  $M_W$  5.9 Southeast  
76 Off-Mie, Japan, earthquake (Kubo et al., 2019). Such characteristics of high-frequency ground  
77 motions are usually attributed to the nonlinear soil response associated with an increase in  
78 damping and a reduction in shear modulus for large shear strain (Bresnev and Wen, 1996). It is  
79 worth noting that low-rise buildings on soil sites may experience less damage due to the  
80 significant reduction of high-frequency ground motions (Trifunac and Todorovska, 1998).

81

82 However, it is still unclear how properties of near-surface materials, including seismic wave  
83 velocities, Poisson's ratio, and attenuation parameters, contribute to the variability in site  
84 responses to seismic waves and whether the velocity structure underneath soil sites may cause  
85 the depletion of high-frequency energy in HVSRs. The classification of near-surface site  
86 conditions is primarily based on the time-averaged shear wave velocity of the top 30 m of the  
87 crust (Park and Elrick, 1998),  $V_{S30}$ , which is shown to correlate with geologic units in California  
88 (Wills et al., 2000) and ground motion amplification (Field, 2000). For broad site-classifications  
89 used by National Earthquake Hazards Reduction Program (NEHRP), rock sites should have  $V_{S30}$   
90 larger than 760 m/s, whereas soil sites can be further classified to soft soil (site class E,  $V_{S30} \leq$   
91  $180 \text{ m/s}$ ), stiff soil (site class D,  $180 < V_{S30} \leq 360 \text{ m/s}$ ), and very dense soil (site class C,  
92  $360 < V_{S30} \leq 760 \text{ m/s}$ ) (BSSC, 2001).

93

94 The low  $V_{S30}$  of soil sites leads to Poisson's ratios considerably larger than 0.25, the value for a  
95 perfectly isotropic elastic material, since the compressional wave velocity ( $V_p$ ) is not reduced at  
96 the same rate as the shear wave velocity ( $V_s$ ) for shallow depths. Brocher (2005) has compiled  
97  $V_p$  and  $V_s$  from borehole logs, vertical seismic profiles, laboratory measurements, and  
98 tomography studies for a variety of rocks, primarily in California. The data shows that  $V_s$  varies  
99 more rapidly with  $V_p$  when  $V_p$  is less than 3.75 km/s, resulting in Poisson's ratios between 0.25  
100 and 0.5 in the shallow crust (e.g., top 1-2 km). Especially for young, saturated sediments, the  
101 Poisson's ratio approaches 0.5 as  $V_s$  quickly drops to 100 m/s when  $V_p$  is reduced to 1500 m/s.  
102 Based on the empirical relationship between  $V_p$  and  $V_s$  (equation (9) in Brocher, 2005), soil sites  
103 with  $V_{S30}$  less than 760 m/s should have Poisson's ratios larger than 0.43. Taking into  
104 consideration large Poisson's ratios at shallow depths can help improve the stability of  
105 hypocenter determination (Nicholson and Simpson, 1985).

106

107 Another factor that can strongly affect ground motions is seismic wave attenuation of near-  
108 surface materials, quantified by the  $Q$  values. Based on the borehole data of local earthquakes in  
109 California, Abercrombie (1997) showed that over 90% of the attenuation occurs within the upper  
110 3 km, and the near-surface  $Q$  is very low (i.e.,  $Q_p \sim 26$  and  $Q_s \sim 15$  in the upper 300 m). The study  
111 concluded that the near-surface attenuation has a weak dependence on site conditions, as  $Q$  is  
112 more sensitive to fracture density, temperature and fluid content rather than rock types. Other  
113 studies (e.g., Bethmann, 2012; Edwards and Fah, 2013; Wang, 2016) also found similar  
114 attenuation parameters for soil and rock sites in Europe, Middle East and Asia. However, the 3-D  
115 attenuation models of the southern California crust reveal low  $Q_p$  and  $Q_s$  values in the top 1 km  
116 layer of major sedimentary basins and high  $Q$  zones that correspond to the high-velocity rocks of  
117 the mountain ranges (Hauksson and Shearer, 2006). Van Houtte et al. (2011) also validated the  
118 correlation between  $V_{S30}$  and the high-frequency decay parameter  $\kappa$  using ground motion data  
119 from both the Kiban-Kyoshin network (KiK-net) in Japan and the Next Generation of  
120 Attenuation (NGA) database. Neighbors et al. (2015) showed that  $\kappa$  estimated from the 2010  
121 Maule, Chile aftershocks exhibits site-condition dependence, but the overlap of error bars of  
122 attenuation parameter measurements suggests the difference between hard rock and soil sites  
123 may be insignificant.

124

125 The observed low  $V_s$ , large Poisson's ratio, and possible low  $Q_s$  of soil sites encourage the  
126 hypothesis that they may partially contribute to the features of high-frequency ground motions.  
127 3D velocity models with low  $V_s$  and large Poisson's ratios for soil sites are commonly  
128 implemented in kinematic ground motion simulations (e.g., Olsen, 2000; Frankel, 2009;  
129 Aagaard, 2010; Taborda and Bielak, 2014; Asano, 2016; Pitarka, 2016; Rodgers, 2018), though  
130 there is still a limitation in the lowest  $V_s$  that can be resolved. However, due to the lack of  
131 observational constraints or for computational convenience, ground motion simulations may also  
132 assume a constant Poisson's ratio inside the sedimentary basin that is much lower than observed  
133 values (e.g., Meza-Fajardo, 2016) or velocity models with a few layers. Some kinematic ground  
134 motion simulations also explicitly consider the reduction of stiffness during nonlinear soil  
135 deformation by correcting site responses (e.g., Esmailzadeh et al., 2019; Rodgers et al., 2020).

136

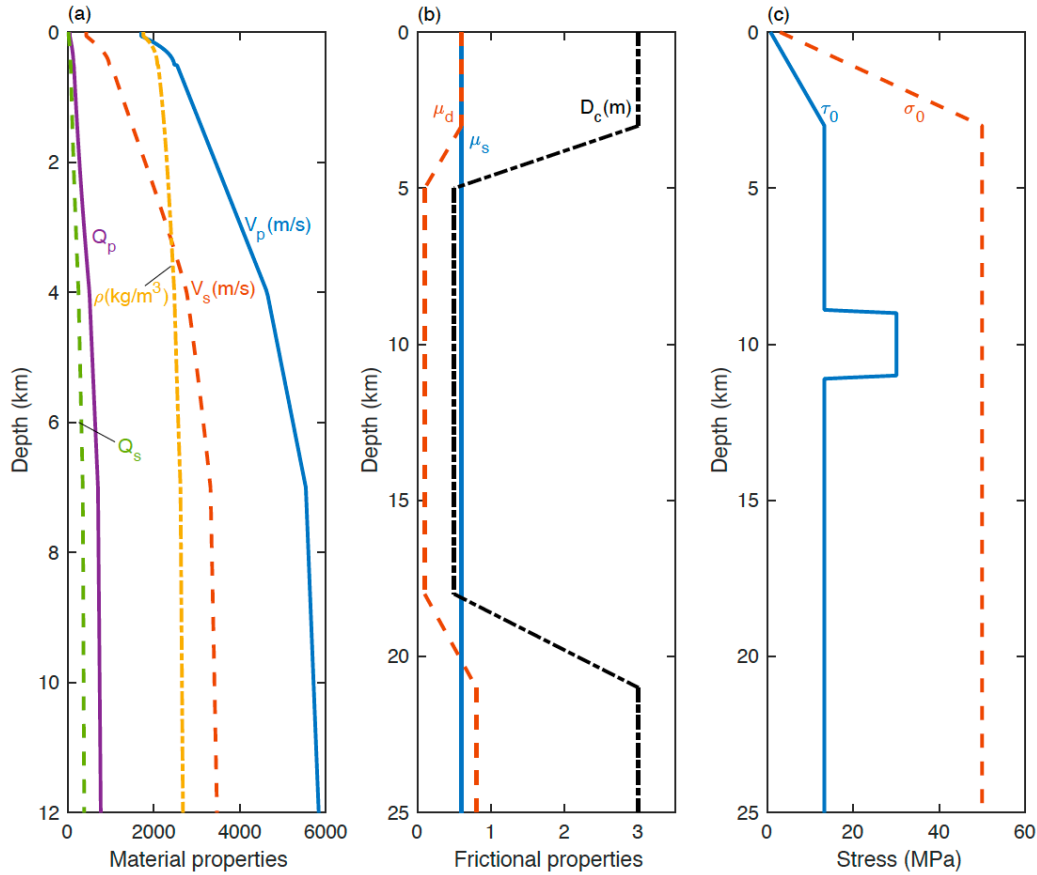
137 Motivated by the contrasting behaviors of HVSRs on soil and rock sites in the recent Ridgecrest  
138 earthquake (Hough et al., 2020), we characterize the contributions of shallow velocity structure  
139 to the differences of ground motion amplitudes, frequency contents and HVSRs on soil and rock  
140 sites by simulating 2-D dynamic rupture propagating on a vertical 1-D fault. Dynamic rupture  
141 simulations calculate kinematic rupture processes of earthquakes by respecting fault physics and  
142 considering the interaction between fault stress and frictional strength as well as seismic wave  
143 propagation in the surrounding medium, leading to realistic scenarios of strong ground motions  
144 (e.g., Harris et al., 2018). Using dynamic rupture simulations helps differentiate the respective  
145 contributions of earthquake source and seismic wave propagation, which are both affected by the  
146 velocity structure and attenuation parameter. In the Methodology section, we discuss the velocity  
147 model, attenuation parameters, stresses and frictional parameters used in dynamic rupture  
148 simulations. In the Results section, we present the source characteristics of simulated rupture  
149 (e.g., slip, slip rate and rupture speed), and compare the acceleration waveforms and HVSRs  
150 recorded on soil and rock sites. We show that a smooth velocity model combined with low  $V_s$   
151 can give rise to diminished amplitudes of high-frequency HVSRs in soil simulations.

152

## 153 **Methodology**

154

155



156  
 157 Figure 1. Depth variations of (a) material properties, (b) frictional parameters, and (c) fault stresses in  
 158 model S. Model R uses the same fault friction and stresses as shown in (b) and (c).

159  
 160 In both 2-D dynamic rupture simulations and point-source models, we use a 1-D velocity model  
 161 derived from empirical relationships between seismic wave velocities and depths in northern  
 162 California (Brocher, 2008). Since Holocene and Plio-Quaternary deposits can greatly amplify  
 163 ground motions in northern California, we adopt the depth variations of seismic wave velocities  
 164 for Holocene and Plio-Quaternary sedimentary rocks at depths less than 500 m and for older  
 165 Cenozoic sedimentary rocks at depths more than 500 m (Table 1; Figure 1a). Since the maximum  
 166 resolvable frequency of ground motions is determined by the slowest seismic wave velocity in  
 167 the simulations,  $V_p$  and  $V_s$  in the top 60 m are kept constant and equal to the values at 60 m  
 168 depth to resolve ground motions at high frequencies. Given  $V_{S30}=436$  m/s, the site condition is  
 169 classified as a very dense soil. We refer to this velocity model as model S (“S” stands for soil)  
 170 for the rest of the paper. The Poisson’s ratio in model S can be calculated from  $\frac{(V_p/V_s)^2-2}{2(V_p/V_s)^2-2}$  using  
 171  $V_p$  and  $V_s$  in Table 1. To compare ground motions recorded at soil and rock sites, we use a

172 different 1-D velocity model based on the same  $V_p$  vs. depth relationship, but with a Poisson's  
 173 ratio of 0.25. Hence,  $V_{S30}=988$  m/s in this velocity model, and the site condition is classified as a  
 174 rock site. We refer to this velocity model as model R ("R" stands for rock) for the rest of the  
 175 paper. The major difference between velocity models S and R lies at depths shallower than 3 km,  
 176 where  $V_s$  is significantly lower in model S.

177

178 **Table 1. Depth variations of  $V_p$  and  $V_s$  for simulated soil sites**

Depth $z$ (km)	$V_p$ (km/s)	$V_s$ (km/s)
$0 < z < 0.06$	$V_p = 1.711$	$V_s = 0.436$
$0.06 \leq z < 0.5$	$V_p = 1.5 + 3.735z - 3.543z^2$	$V_s = 0.7858 - 1.2344V_p +$ $0.7949V_p^2 - 0.1238V_p^3 +$ $0.0064V_p^4$
$0.5 \leq z < 4$	$V_p = 2.24 + 0.6z$	
$4 \leq z < 7$	$V_p = 4.64 + 0.3(z - 4)$	
$7 \leq z < 12$	$V_p = 5.54 + 0.06(z - 7)$	

179

180 We calculate density from  $V_p$  using the Nafe-Drake curve (Brocher, 2005; Ludwig et al., 1970).  
 181 We estimate  $Q_s$  from  $V_s$  using the relationship ( $Q_s = -16 + 104.13V_s - 25.225V_s^2 + 8.2184V_s^3$   
 182 for  $0.3 \text{ km/s} < V_s < 5 \text{ km/s}$ ) constrained by the forward modeling of strong ground motions  
 183 from the 1994 Northridge earthquake (Brocher, 2008; Graves and Pitarka, 2004).  $Q_p$  is assumed  
 184 to be twice the value of  $Q_s$  (Brocher, 2008). Similar to seismic wave velocities,  $Q_p$  and  $Q_s$  are  
 185 kept constant in the top 60 m ( $Q_p=50$  and  $Q_s=25$ ). We also investigate the effects of the same  
 186 attenuation profiles for soil and rock simulations in the Results section, given the possible weak-  
 187 dependence of near-surface attenuation on site conditions (Abercrombie, 1997; Bethmann,  
 188 2012; Edwards and Fah, 2013; Wang, 2016).

189

190 We simulate along-dip rupture propagation as mode II rupture on a 1-D vertical fault governed  
 191 by a linear slip-weakening friction law (Ida, 1972; Andrews, 1976a), which describes the drop of  
 192 friction coefficient from the static level  $\mu_s$  to the dynamic level  $\mu_d$  when slip reaches the critical  
 193 slip distance  $D_c$  (Figure 1b). A free surface is applied to the top boundary of the modeling  
 194 domain, whereas the other boundaries are absorbing boundaries (Clayton and Engquist, 1977).  
 195 Synthetic waveforms are calculated on the surface at distances of 5, 10 and 15 km from the fault.

196 The station-fault distances are chosen to be similar to those in the ground motion analysis of the  
197 2019 Ridgecrest earthquake (Hough et al., 2020).

198

199 Frictional parameters and fault stresses vary along depth in our simulations. Both  $\mu_d$  and  $D_c$  are  
200 constant at seismogenic depths (5-18 km), but increase at shallower and deeper parts to allow  
201 earthquake rupture to stop (Figure 1b). Note that using  $D_c = 1m$  at shallow depths does not have  
202 a significant impact on the resulting earthquake rupture and ground motions at the distances  
203 considered in this study (i.e., 5-15 km), but the choice of  $D_c$  can have a large effect on ground  
204 motions at distances closer to the fault (e.g., Wang et al., 2019). Effective normal stress  $\sigma_o$   
205 increases linearly with depth for the first 3 km and remains a constant value of 50 MPa for the  
206 rest of the fault (Figure 1c). Initial shear stress  $\tau_o$  follows the variation of effective normal stress  
207 except inside the nucleation zone to keep an S ratio of 2 ( $S = \frac{\mu_s \sigma_o - \tau_o}{\tau_o - \mu_d \sigma_o}$ ). Dynamic rupture is  
208 nucleated at a depth of 10 km by a 2 km long overstressed patch with the initial shear stress  $\tau_o$   
209 0.3% higher than the static shear strength  $\mu_s \sigma_o$ . As rupture propagates, it radiates seismic waves  
210 that propagate to the surrounding medium, which generates ground motions.

211

212 Dynamic rupture is solved numerically using a spectral element method (SEM2DPACK, Ampuero,  
213 2009). We require at least 5 GLL nodes in the process zone to resolve the reduction from the static  
214 friction to dynamic friction during rupture propagation. To resolve ground motions at a maximum  
215 frequency of 6 Hz, we use 75 m element with 5 GLL nodes, so there are at least 5 nodes for the  
216 minimum wavelength in the simulations. The resolution test shows that in fact ground motions can  
217 be resolved to a maximum frequency of 7-8 Hz for 75 m element. Thus, our results are shown up  
218 to a maximum frequency of 7 Hz. We allow frequency-independent seismic attenuation in the  
219 simulations by adding viscoelastic terms in the stress-strain relations (Moczo et al., 2004). Three  
220 anelastic functions and relaxation frequencies are used to produce an approximately flat Q between  
221 0.1 and 10 Hz. The details of the implementation of attenuation in dynamic rupture simulations  
222 are shown by Huang et al. (2014). For frequencies higher than 1 Hz, Q can be an increasing  
223 function of frequency and is modeled by the form of a power law (Withers et al., 2015), though  
224 the frequency-dependence of Q may affect ground motions on soil and rock sites in a similar  
225 fashion.

226



## 227 **Results**

228

229 In this section, we present dynamic rupture scenarios and resulting ground accelerations for soil  
230 and rock simulations that have different velocity models and attenuation parameters. We discuss  
231 in more detail how the velocity models and attenuation parameters can change the variation of  
232 horizontal-to-vertical spectral ratios and address why a depletion of high-frequency energy is  
233 observed on soil. We also show how rupture styles (buried vs. surface rupture), double-couple  
234 point sources and new shallow velocity structure affect ground motions on soil and rock sites.

235

### 236 *Dynamic rupture simulations*

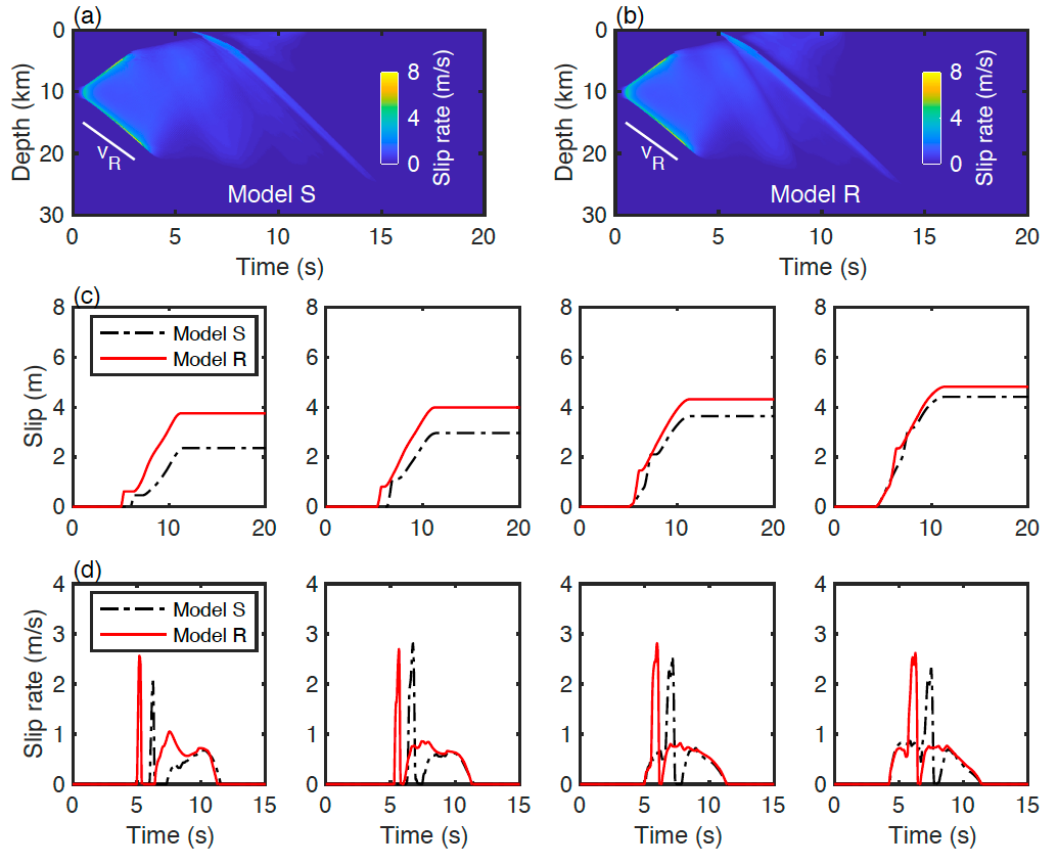
237

238 The values of fault friction and stresses in our simulations allow dynamic rupture to propagate at  
239 nearly Rayleigh wave speed in both up-dip and down-dip directions shortly after nucleation  
240 (Figures 2a and b). Different velocity models have a negligible effect on rupture speed, slip and  
241 slip rate for depths larger than 3 km. The largest final slip is  $\sim 11$  m located near the hypocenter  
242 depth (10 km). If we define the along-dip rupture width as the region where slip is greater than  
243 1 % of the maximum final slip, rupture width is  $\sim 24$  km in both models. Assuming that the  
244 rupture length is equal to the rupture width, and slip at a given depth is the same along strike,  
245 simulated rupture generates earthquakes of magnitude  $\sim 7.3$  for both model S and model R. Note  
246 that the magnitude calculated from the 2-D model is larger than the magnitude of a real  
247 earthquake with the same rupture area and peak slip, since the peak slip is assumed to extend  
248 along strike in our magnitude calculation.

249

250 At shallow depths, however, model S and model R exhibit different earthquake source  
251 properties. Rupture becomes significantly slower as it propagates through the shallow part of the  
252 fault for model S and results in smaller slip due to lower  $V_s$ . A detailed inspection of final slip  
253 shows that surface slip is only one-third of that for model R, and slip at 1 km depth is about two-  
254 thirds of that for model R. The difference in final slip gradually decreases with depth (Figure 2c).  
255 Moreover, slip rate functions have multiple fluctuations and contain a mixture of sharp and  
256 smooth slip pulses for both models (Figure 2d). The spatiotemporal slip rate distribution (Figures  
257 3a and b) reveals that the sharp slip pulse, a most noticeable feature in the slip rate function at

258 shallow depths, originates from the surface S-wave reflection. Hence, sharp pulses appear earlier  
 259 in slip rate functions of model R given its higher  $V_s$  at shallow depths. The smooth pulse  
 260 following behind the sharp pulse has a larger average slip rate at shallow depths in model R, and  
 261 rise time (i.e, the duration of slip rate function) is longer especially for depths shallower than 1  
 262 km. These two effects together contribute to larger shallow slip of model R.  
 263



264  
 265 Figure 2. Comparison of (a and b) spatiotemporal distribution of slip rate, (c) slip and (d) slip rate (low-  
 266 pass filtered at 4 Hz) for model S and model R. (c) and (d) show results at depths of 1, 2, 3 and 4 km from  
 267 left to right.

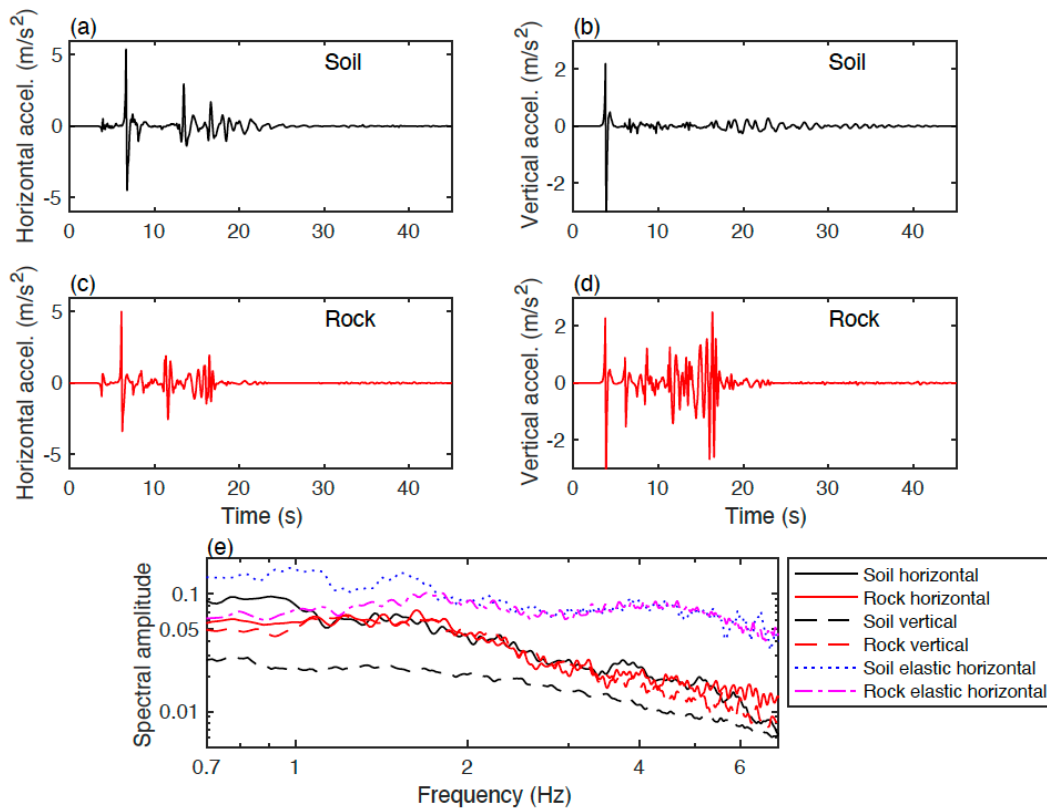
268

269 ***Seismic acceleration waveform and spectra***

270

271 The previous section shows that the lower  $V_s$  in model S results in smaller slip and slower  
 272 rupture speed at the shallow part of the fault, but the overall characteristics of rupture  
 273 propagation are very similar between the two models at depths larger 3 km, where most seismic  
 274 energy is radiated. Near-fault ground motions from these two rupture scenarios, however, exhibit

275 distinct features, suggesting that different velocity models have a more significant influence on  
 276 the propagation of seismic waves to near-fault stations. This important role of velocity models is  
 277 further validated in sections “Buried rupture vs. surface rupture” and “Point-source models of  
 278 ground motions on soil and rock sites” for which rupture properties are either very similar  
 279 throughout the fault or the same for different models. Figure 3 demonstrates ground acceleration  
 280 recorded at a distance of 10 km from the fault. Both horizontal and vertical acceleration last for a  
 281 longer duration on soil than on rock. Peak horizontal acceleration on soil is slightly larger than  
 282 on rock, whereas peak vertical acceleration on soil is slightly lower. Vertical acceleration  
 283 waveforms on soil and rock also have distinct characteristics. Vertical acceleration on soil stays  
 284 at low amplitudes after the P-wave arrival, while vertical acceleration on rock has multiple large-  
 285 amplitude peaks with the largest peak arriving at  $\sim 13$ s after the P-wave arrival.  
 286



287  
 288 Figure 3. Plots of (a-d) simulated acceleration waveforms and (e) spectra for soil and rock sites at a  
 289 distance of 10 km from the fault for surface rupture. The dotted and dash-dot lines show acceleration  
 290 spectra for elastic soil and rock simulations.

291  
 292

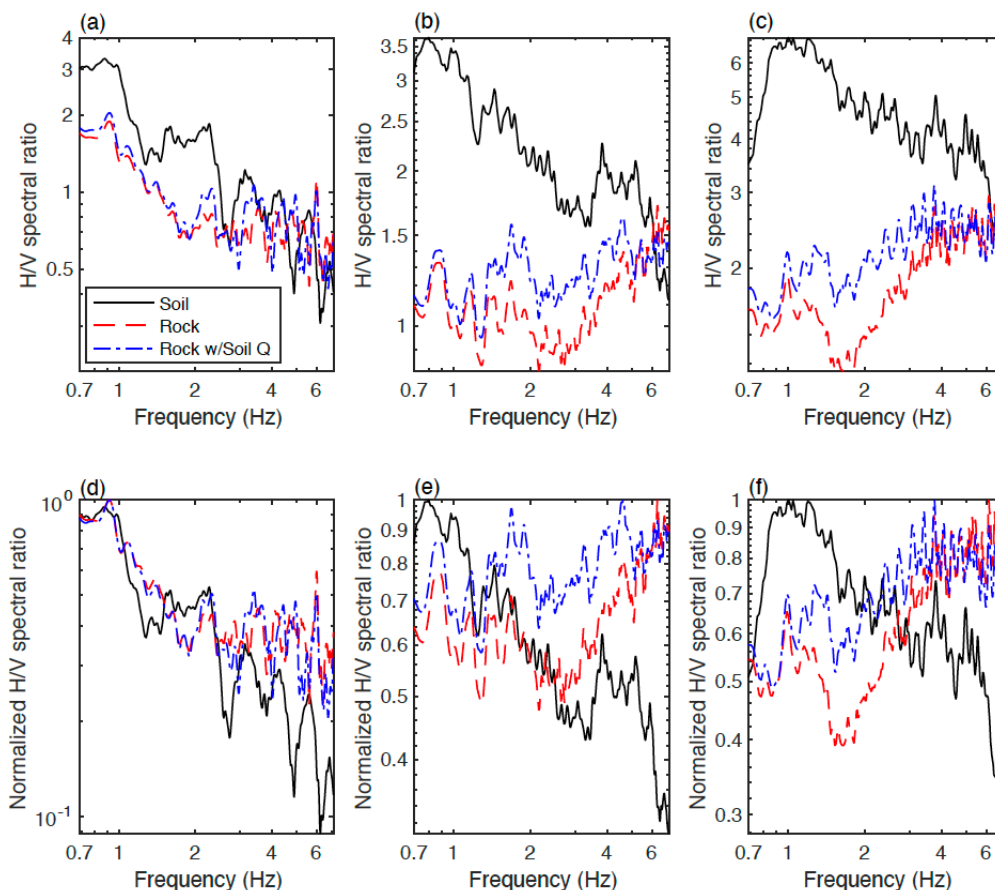
293 To understand the frequency-dependence of near-field ground motions, we calculate acceleration  
294 spectra by taking a Fourier transform of the 45 s acceleration records (Figure 3e). The spectra are  
295 smoothed using a 30-point moving average. For soil sites, we find spectral amplitudes of  
296 horizontal acceleration are considerably larger than those of vertical acceleration for the whole  
297 frequency band of interest (0.7-7 Hz). For rock sites, spectral amplitudes of horizontal  
298 acceleration are, on average, slightly larger than those of vertical acceleration at frequencies less  
299 than 1 Hz and higher than 4 Hz. Spectral amplitudes of horizontal and vertical components on  
300 rock become indistinguishable at 1-4 Hz.

301  
302 Comparing horizontal acceleration spectra recorded by soil and rock sites, we find soil sites  
303 amplify near-field horizontal ground acceleration only at low frequencies. The horizontal  
304 spectral amplitude on soil is higher by about a factor of 1.7 at 0.7 Hz than on rock. At  
305 frequencies higher than 1.1 Hz, there is no significant difference between the soil and rock sites  
306 in horizontal spectral amplitudes, which agrees qualitatively with the finding by Joyner and  
307 Boore (1988). They suggested that similar horizontal high-frequency acceleration amplitudes for  
308 soil and rock sites can result from the suppression of high-frequency amplification by attenuation  
309 in the soil. However, our rupture simulations in a purely elastic medium, in which attenuation  
310 effects are not considered, still show similar horizontal acceleration amplitudes at higher  
311 frequencies for soil and rock sites (dotted and dash-dot lines in Figure 3e).

### 312 313 *Horizontal-to-vertical spectral ratios (HVSRs)*

314  
315 We then calculate HVSRs for stations at distances of 5, 10 and 15 km on soil and rock sites  
316 (Figure 4). To further investigate the effects of attenuation parameters, we also simulate ground  
317 motions from a rock model with the same attenuation parameters as the soil model (dash-dot  
318 lines in Figure 4), i.e., smaller  $Q_p$  and  $Q_s$  at shallow depths than the previous rock model.  
319 However, we find the difference between HVSRs on soil and rock sites has a weak dependence  
320 on attenuation parameters. Overall, HVSRs on soil are higher than those on rock at low  
321 frequencies. For the station at 5 km from the fault, HVSRs on soil approach those on rock at  
322 frequencies higher than 3 Hz. For the station at 10 km from the fault, HVSRs on soil become  
323 lower than those on rock at frequencies higher than 6 Hz. HVSRs on soil also share similar

324 features at different stations: Their amplitudes are the largest at  $\sim 1$  Hz and gradually decrease at  
 325 higher frequencies. For the station at 10 km from the fault, HVSRs on soil are higher by a factor  
 326 of  $\sim 3$  at 1 Hz and by a factor of  $\sim 2$  at 3 Hz than on rock.  
 327



328  
 329 Figure 4. Plots of (a-c) simulated HVSRs and (d-f) normalized HVSRs for soil and rock sites at distances  
 330 of (a and d) 5, (b and e) 10 and (c and f) 15 km from the fault for surface rupture. The dashed lines show  
 331 results from a rock simulation with different attenuation parameters from the soil simulation, whereas the  
 332 dash-dot lines show results from a rock simulation with the same attenuation parameters as soil.  
 333

334 To investigate the frequency-dependence of HVSRs, we normalize them by the maximum  
 335 amplitudes for the frequency band of interest. The normalized HVSRs clearly show that high-  
 336 frequency content is relatively richer on rock than on soil (Figure 4). This simulation result is  
 337 qualitatively similar to the observed reduced amplitudes of high-frequency HVSRs at deep  
 338 alluvium sites for the recent Ridgecrest earthquake (Hough et al., 2020). It is worth noting that  
 339 for the stations at 10 and 15 km distances, HVSRs on rock do not decay at high frequencies as

340 observed in real data, but rather increase in amplitudes. An even steeper increase in HVSRs at  
341 high frequencies may be observed in simulations if  $Q$  is modeled as an increasing function of  
342 frequency (Withers et al., 2015). As discussed later, reproducing the exact behaviors of high-  
343 frequency HVSRs may require 3D rupture simulations or small-scale velocity heterogeneity that  
344 can generate more scattering of seismic waves.

345

### 346 *What causes the depletion of high-frequency energy on soil?*

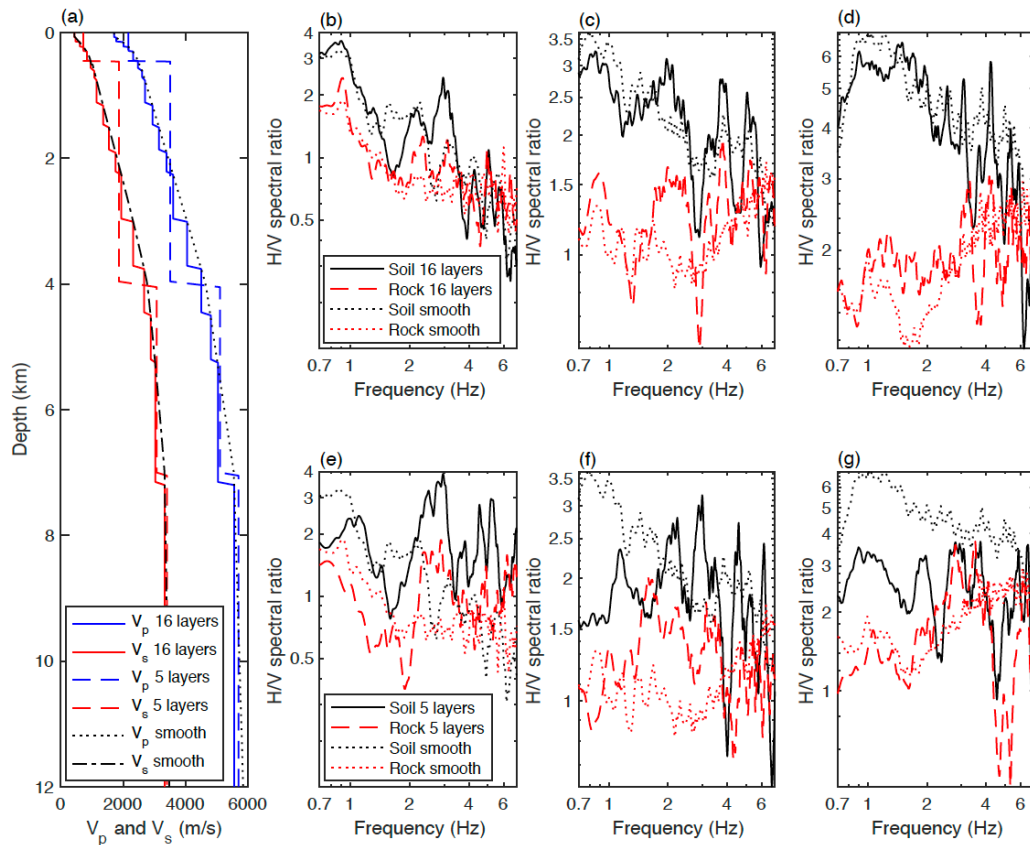
347

348 Our analysis shows that low  $V_s$  and large Poisson's ratio of the shallow crust contribute to the  
349 amplification of low-frequency horizontal ground motions on soil, but it is intriguing why high-  
350 frequency horizontal ground motions are not similarly amplified as their low-frequency  
351 counterpart. The attenuation effect does not seem to play a role, as elastic simulations also  
352 produce similar horizontal acceleration amplitudes on soil and rock at higher frequencies (dotted  
353 and dash-dot lines in Figure 3e). Besides the difference in  $V_s$ , the velocity models in our  
354 simulations have smooth velocity gradients, governed by the empirical relationships between  
355 seismic wave velocities and depths (Brocher, 2008). We hypothesize that a smooth velocity  
356 gradient may not be as efficient as a 1-D layer model in amplifying high-frequency energy, since  
357 the velocity change within the wavelength that corresponds to a given high frequency would be  
358 small for a smooth velocity gradient.

359

360 To test this hypothesis, we generate two 1-D layer models with seismic velocities directly  
361 derived from the smooth velocity gradient (Figure 5). In the first model, we use 16 layers to  
362 closely mimic the smooth velocity gradient. In the second model, we define 5 velocity layers  
363 with the same boundaries (i.e., 0.5, 4, 7 and 12 km) used by Brocher (2008) to derive the  
364 empirical relationships. We then represent the seismic velocity for each layer using the median  
365 seismic velocity. The density and attenuation parameters are derived in the same way. We find  
366 that HVSRs on soil still decay at high frequencies for the 16-layer velocity model, and the  
367 contrasting behaviors of soil and rock sites are similar as the smooth velocity model. For the 5-  
368 layer velocity model, however, HVSRs on soil do not show a clear decay as frequency increases  
369 and have comparable amplitudes at low and high frequencies. The different outcomes of the 1-D  
370 layer models suggest that a smooth velocity gradient or a velocity model with sufficient layers to

371 mimic a smooth velocity gradient plays a critical role in the depletion of high-frequency energy  
 372 on soil in our simulations.  
 373



374  
 375 Figure 5. Illustrations of (a) the depth variation of seismic wave velocities for the 16-layer velocity model  
 376 (solid lines) and the 5-layer velocity model (dashed lines) compared to the smooth velocity gradient  
 377 (dotted and dash-dot lines), as well as (b-g) simulated HVSRs for soil and rock sites at distances of (b  
 378 and e) 5, (c and f) 10 and (d and g) 15 km from the fault for the 16-layer and 5-layer velocity models (solid  
 379 and dashed lines) compared to the simulated HVSRs for soil and rock sites in smooth velocity models  
 380 (dotted lines).

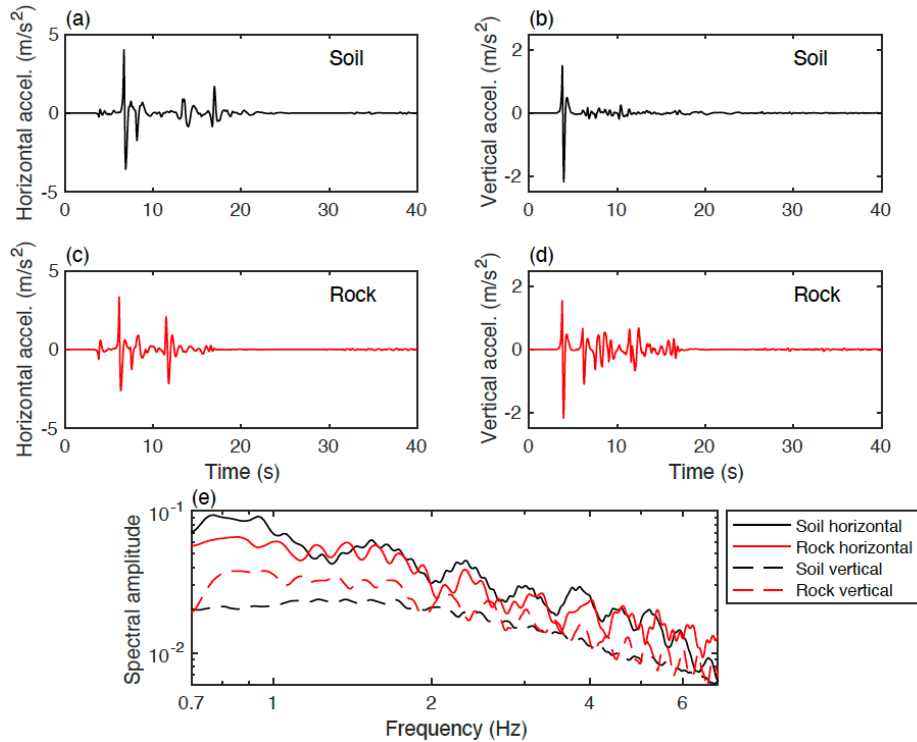
381

382 ***Buried rupture vs. surface rupture***

383

384 Fault stress and frictional conditions in previous simulations allow rupture to reach the surface.  
 385 Ground motion observations suggest that surface rupture and buried rupture can have a strong  
 386 influence on the characteristics of ground motions. For example, ground motions generated by  
 387 surface rupture are weaker than buried rupture for a period range of 0.3-3 sec (Somerville, 2003).  
 388 Such difference in ground motions can be attributed to a shallow weak zone as well as the larger

389 stress drop and deeper hypocenter of buried rupture (Pitarka, et al., 2009). Here we investigate  
 390 how buried rupture influences the observed acceleration waveform and spectral features. The  
 391 comparison between surface rupture and buried rupture also helps us understand how rupture  
 392 propagation in the shallow crust affects the ground motion difference between soil and rock sites.  
 393



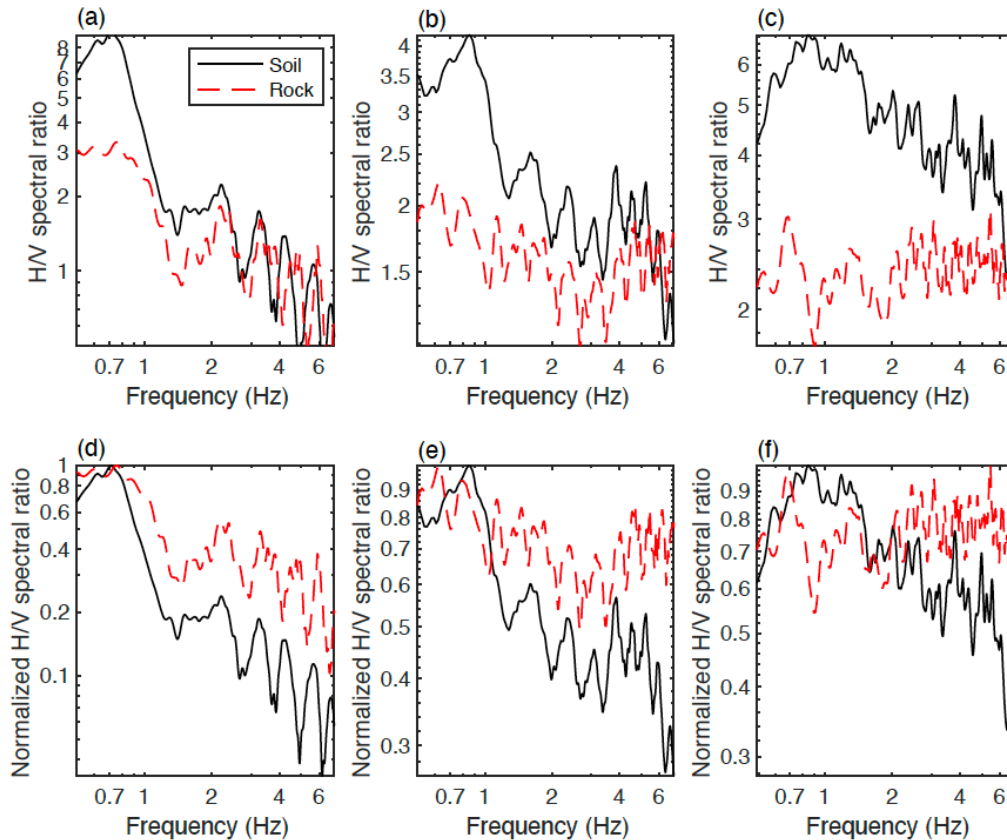
394  
 395 Figure 6. Plots of (a-d) simulated acceleration waveforms and (e) spectra for soil and rock sites at a  
 396 distance of 10 km from the fault for buried rupture.

397  
 398 To simulate buried rupture, we increase  $\sigma_o$ ,  $\mu_d$  and  $D_c$  in the top 3 km to values that prevent  
 399 rupture from reaching the surface for both velocity models. The buried rupture models have  
 400 similar rupture properties at shallow depths. The resulting slip is less than 0.2 m for the top ~ 1  
 401 km and is zero near the surface. Magnitudes of simulated earthquakes are ~7.2, slightly smaller  
 402 than the surface-rupturing scenarios. Near-source acceleration records of buried rupture show  
 403 similar waveform features to surface rupture for the first 10 s after the P-wave arrival (Figure 6),  
 404 but wave reverberations afterwards seem to be less pronounced on both soil and rock for buried  
 405 rupture. On soil sites, since the lack of wave reverberations affects the apparent total duration of  
 406 ground motions, spectral amplitudes of horizontal and vertical acceleration are slightly reduced  
 407 at 0.7 Hz (Figure 6). On rock sites, the lack of wave reverberations after the first 10 s has



408 significantly reduced ground motions, especially for the vertical component. Note that the peak  
 409 vertical acceleration on rock arrives at 13 s after the P-wave arrival for surface rupture (Figure  
 410 3). Compared to surface rupture, spectral amplitudes of vertical acceleration on rock are reduced  
 411 by almost a half for buried rupture (Figure 6). As a result, the HVSRs on rock are also larger for  
 412 buried rupture (Figure 7).

413



414

415 Figure 7. Plots of (a-c) simulated HVSRs and (d-f) normalized HVSRs for soil and rock sites at distances  
 416 of (a and d) 5, (b and e) 10 and (c and f) 15 km from the fault for buried rupture.

417

418 The larger HVSRs for buried rupture (Figure 7), however, do not affect previous results  
 419 regarding the difference of HVSRs on soil and rock. The results from buried rupture confirm the  
 420 finding that different velocity models, rather than rupture processes, have a major influence on  
 421 the contrasting behaviors of ground motions on soil and rock. For the station at 5 km distance,  
 422 HVSRs on soil and rock are both increased by a factor of  $\sim 2$  for buried rupture compared to the  
 423 values for surface rupture at low frequencies. Thus, HVSRs on soil are still higher by a factor of  
 424 2-3 for frequencies around 0.7 Hz. For the station at 10 km distance, HVSRs on soil are higher

425 by a factor of  $\sim 2$  than on rock for frequencies around 1 Hz. Normalized HVSRs also support  
 426 richer high-frequency energy on rock than on soil (Figure 7). The contrast between normalized  
 427 soil and rock HVSRs at 5 km distance is even larger for buried rupture than for surface rupture,  
 428 especially for frequencies higher than 1.5 Hz.

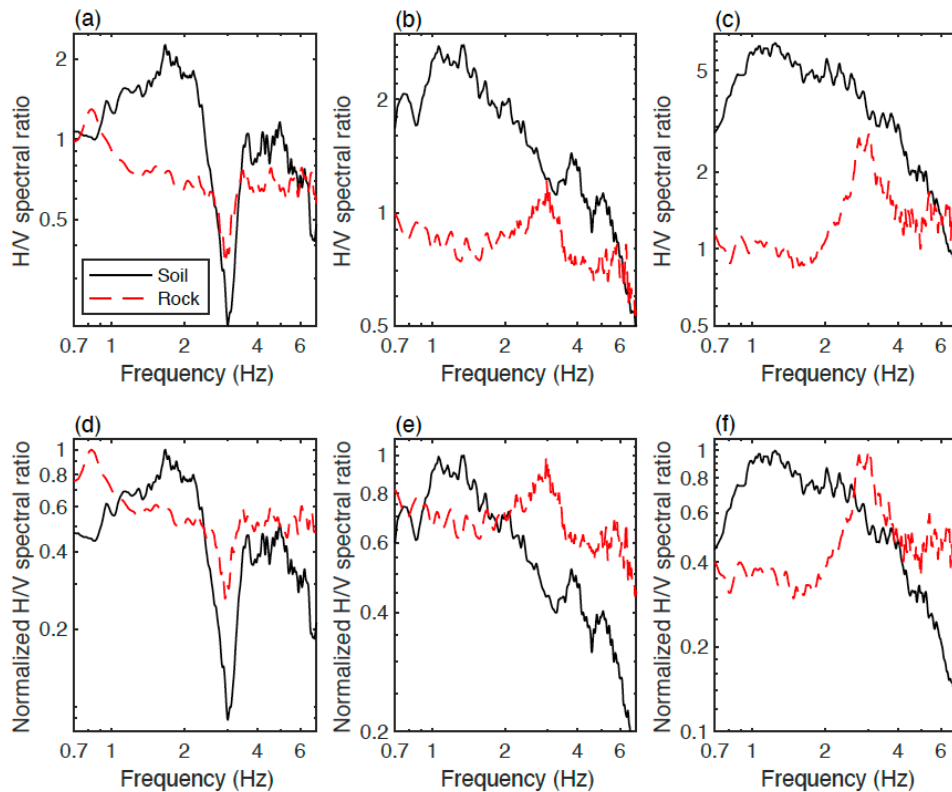
429

430 ***Point-source models of ground motions on soil and rock sites***

431

432 Our dynamic rupture simulations have demonstrated that different velocity structure underneath  
 433 soil and rock sites have a critical impact on high-frequency ground motions. Here we show that  
 434 the contrasts of HVSRs on soil and rock sites can also be observed in point-source models, in  
 435 which the earthquake is represented by a double-couple source with a dip angle of  $90^\circ$  and a  
 436 Gaussian source time function. The central frequency of the source time function is 1 Hz, which  
 437 is near the corner frequencies of  $M_w \sim 5$  earthquakes. The source properties of earthquakes are  
 438 the same for both soil and rock models.

439



440

441 Figure 8. Plots of (a-c) simulated HVSRs and (d-f) normalized HVSRs for soil and rock sites at distances  
 442 of (a and d) 5, (b and e) 10 and (c and f) 15 km from the fault for a double-couple source.

443

444 Similar to dynamic rupture results, the simulated HVSRs on soil sites are significantly larger  
445 than those on rock sites at low frequencies (Figure 8). The difference of HVSRs on rock and soil  
446 sites is especially large at 1-2 Hz for all the stations. HVSRs on soil gradually decay and  
447 approach those on rock at high frequencies. The normalized HVSRs also support richer high-  
448 frequency content in HVSRs on rock sites, though the HVSRs calculated from a point source  
449 appear to have a bump around 3 Hz for rock sites. Given the same earthquake source properties  
450 in point-source models, they demonstrate that the amplified low-frequency HVSRs and the rapid  
451 decay of HVSRs at high frequencies on soil sites are primarily the result of the smooth velocity  
452 structure.

453

#### 454 *New velocity models for the top 60 m*

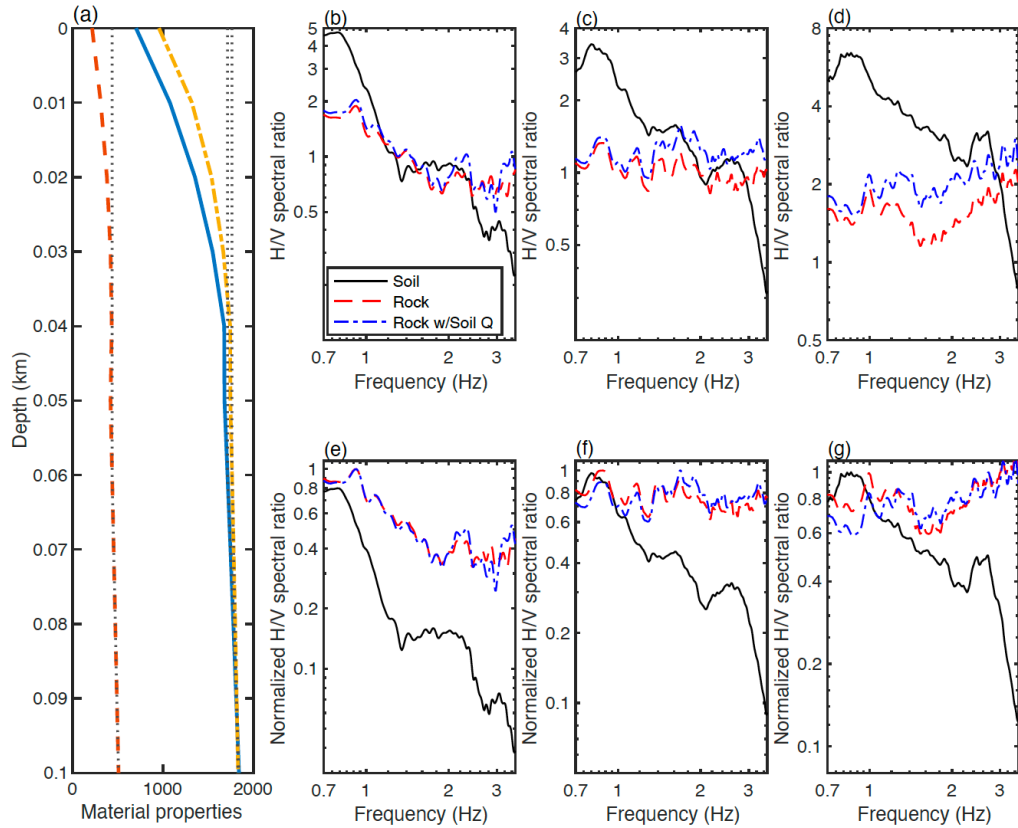
455

456 One remaining question in our dynamic rupture simulations is the effect of the velocity structure  
457 for the top 60 m. In previous simulations, seismic velocities are kept constant at this depth range  
458 to accurately calculate ground motions at a maximum frequency of 7 Hz with reasonable  
459 computational costs. In this section, we relax this particular model constraint and allow material  
460 properties to vary for the top 60 m.  $V_p$  and  $V_s$  are calculated from their depth variations for  
461 Holocene and Plio-Quaternary deposits at depths less than 60 m (Brocher, 2008). The density  
462 and attenuation parameters are also modified based on their relationships with seismic wave  
463 velocities.  $V_p$ ,  $V_s$ ,  $Q_p$  and  $Q_s$  are 700 m/s, 215 m/s, 26 and 13 at surface, respectively, in the soil  
464 model. Thus, the soil site falls into site class D rather than site class C in the previous models.  
465 Figure 9a illustrates the differences of seismic wave velocities and density between this new  
466 velocity model and previous velocity model for soil sites. For a target maximum frequency of 3  
467 Hz, there are at least 5 nodes for the minimum wavelength in the simulation.

468

469 The most noticeable feature of HVSRs resulting from the new velocity model is an even faster  
470 decay of HVSRs on soil at high frequencies (Figure 9). HVSRs on soil are generally higher than  
471 those on rock at frequencies lower than 1 Hz and decrease to values less than 1 at ~1, 2 and 3 Hz  
472 for stations at 5, 10 and 15 km distances, respectively. HVSRs on soil become lower than those  
473 on rock at frequencies higher than ~2.5 Hz. This interesting finding shows that the frequencies

474 above which a depletion of high-frequency energy is observed in HVSRs also depends on the  
 475 detailed velocity model for the very shallow depths.  
 476



477  
 478 Figure 9. Illustrations of (a) the variation of  $V_p$  (solid line),  $V_s$  (dashed line) and density (dash-dotted line)  
 479 in the new soil velocity model for the top 100 m compared to the previous soil velocity model (dotted  
 480 lines), as well as (b-d) simulated HVSRs and (e-g) normalized HVSRs for soil and rock sites at distances  
 481 of (b and e) 5, (c and f) 10 and (d and g) 15 km from the fault.  
 482

### 483 Discussion and Conclusions

484  
 485 Our dynamic rupture simulations unveil important contribution of velocity models to the  
 486 observed difference in ground motions on soil and rock sites. The low  $V_s$  and large Poisson's  
 487 ratios in the top 3 km of the crust underneath soil sites, in combination with a smooth velocity  
 488 gradient, amplify horizontal ground motions at low frequencies but reduce vertical ground  
 489 motions for the whole frequency range. As a result, HVSRs on soil tend to exhibit larger  
 490 amplitudes than on rock at low frequencies, but HVSRs on soil decay more rapidly than those on  
 491 rock at high frequencies in our simulations.

492  
493 The simulated HVSRs are in qualitative agreement with the observed average HVSRs at deep  
494 alluvium sites for the recent Ridgecrest earthquake (Hough et al., 2020). In the Ridgecrest  
495 observation, HVSRs at deep alluvium sites become lower than those on rock sites at frequencies  
496 above 3 Hz, which is observed for the new shallow velocity model, but not observed when  $V_s$  is  
497 kept constant at 460 m/s for the top 60 m. The better agreement between results from the new  
498 shallow velocity model and the Ridgecrest observation may be related to the fact that they both  
499 assume site class D for soil sites. However, it should also be noted that our dynamic rupture  
500 simulations are not designed to fully capture the rupture characteristics of the Ridgecrest  
501 earthquake given its 2-D nature. For example, the along-strike variation of rupture characteristics  
502 such as rupture directivity can modulate high-frequency ground motions. The exact behaviors of  
503 soil and rock sites can be affected by the azimuths of stations in 3D simulations too. 3D velocity  
504 models, especially those with the addition of small-scale material heterogeneity (Withers et al.,  
505 2019), can cause strong scattering of wave fields and more variability in ground motions.  
506 Though the 2-D rupture simulations may represent the contrasting behaviors of average HVSRs  
507 on soil and rock sites, future investigation should use a more realistic 3-D dynamic rupture  
508 simulation with a full description of earthquake rupture and velocity model to reproduce the  
509 exact behaviors of observed HVSRs.

510  
511 A key point that needs to be emphasized is that the smooth velocity model used in this study  
512 applies to crustal scale, which is fundamental for regional ground motion simulations. However,  
513 the velocity structure for the top 100-200 m can have a significant influence on high-frequency  
514 ground motions too. It has been shown in 1-D site-response models that overly coarse velocity  
515 profiles for the top 100-200 m generate large strain localizations above impedance contrasts  
516 between adjacent layers, which can cause more dissipation of high-frequency energy  
517 (Kaklamanos and Bradley, 2018a; Kaklamanos et al., 2020). This effect is contrary to the effect  
518 of a coarse crustal velocity model in our 2-D dynamic rupture simulations (e.g., the 5-layer  
519 model in Figure 5). The variability of velocity profiles at very shallow depths should also be  
520 accounted for in future dynamic rupture models that simulate high-frequency ground motions.

521

522 Our results have great implications for the understanding of near-field ground motions. The  
523 diminished high-frequency energy in ground motions on soil sites is usually interpreted as a  
524 result of nonlinear sediment response, which reduces high-frequency ground motions by  
525 increasing the damping of ground motions when shear strain increases (Bresnev and Wen, 1996).  
526 Our dynamic rupture simulations demonstrate that a smooth crustal velocity model with low  $V_s$   
527 underneath soil sites can cause different responses of horizontal and vertical ground motions and  
528 at least partially contribute to the depletion of high-frequency energy in the observed HVSRs.  
529 Some 3D ground motion simulations have considered smooth velocity profiles based on a certain  
530 relationship between seismic wave velocities and depths (e.g., Harmsen, 2008), and how high-  
531 frequency ground motions are influenced by smooth 3D velocity models in such simulations  
532 warrants further investigation. Our results support the development of high-resolution velocity  
533 model and provide new physical constraints that can be used to better inform ground motion  
534 simulations.

535

#### 536 **Data and Resources**

537

538 No data were used in this paper. Dynamic rupture is solved using a modified version of  
539 SEM2DPACK (Ampuero, 2009).

540

#### 541 **Acknowledgements**

542

543 The author is grateful to the constructive comments provided by Ruth Harris, who suggested an  
544 important comparison with point source models, and Steve Day, who pointed out the significant  
545 contribution of a smooth velocity gradient that forms the crux of the study. The author also  
546 thanks Editor Jim Kaklamanos, Kyle Withers, an anonymous reviewer, Jing Ci Neo and Olivia  
547 Helprin for their constructive and helpful reviews. This study is supported by the National  
548 Science Foundation through Grant Award 1943742.

549

#### 550 **Declaration of Competing Interests**

551

552 The author acknowledges there are no conflicts of interest recorded.

553

554 **References**

555

556 Aagaard, B. T., R. W. Graves, A. Rodgers, T. M. Brocher, R. W. Simpson, D. Dreger, N. A. Petersson, S.  
557 C. Larsen, S. Ma, and R. C. Jachens (2010). Ground-motion modeling of Hayward fault scenario  
558 earthquakes, Part II: Simulation of long-period and broadband ground motions, *Bull. Seismol. Soc.*  
559 *Am.* **100**, 2945-2977.

560

561 Abercrombie, R. E. (1997). Near-surface attenuation and site effects from comparison of surface and deep  
562 borehole recordings, *Bull. Seismol. Soc. Am.* **87**, 731-744.

563

564 Ampuero, J. P. (2009). SEM2DPACK: A spectral element method tool for 2D wave propagation and  
565 earthquake source dynamics, *User's Guide*, version 2.3.6, Retrieved from [http://www.sourceforge.net/  
566 projects/sem2d/](http://www.sourceforge.net/projects/sem2d/) (last accessed October 2019).

567

568 Andrews, D. J. (1976). Rupture propagation with finite stress in antiplane strain, *J. Geophys. Res.* **81**,  
569 3575-3582.

570

571 Asano, K., H. Sekiguchi, T. Iwata, M. Yoshimi, T. Hayashida, H. Saomoto, and H. Horikawa (2016).  
572 Modelling of wave propagation and attenuation in the Osaka sedimentary basin, western Japan, during the  
573 2013 Awaji Island earthquake, *Geophys. J. Int.* **204**, 1678-1694.

574

575 Beresnev, I. A., and K. L. Wen (1996). Nonlinear soil response—A reality?, *Bull. Seismol. Soc. Am.* **86**,  
576 1964-1978.

577

578 Bethmann, F., N. Deichmann, and P. M. Mai (2012). Seismic wave attenuation from borehole and surface  
579 records in the top 2.5 km beneath the city of Basel, Switzerland. *Geophys. J. Int.* **190**, 1257-1270.

580

581 Brocher, T. M. (2005). Empirical relations between elastic wavespeeds and density in the Earth's  
582 crust, *Bull. Seismol. Soc. Am.* **95**, 2081-2092.

583

584 Brocher, T. M. (2008). Compressional and shear-wave velocity versus depth relations for common rock  
585 types in northern California, *Bull. Seismol. Soc. Am.* **98**, 950-968.

586

587 Building Seismic Safety Council (BSSC) (2001). 2000 Edition, NEHRP Recommended Provisions for  
588 Seismic Regulations for New Buildings and Other Structures, FEMA-368, Part 1 (Provisions): developed  
589 for the Federal Emergency Management Agency, Washington, D.C.

590

591 Clayton, R., and B. Engquist (1977). Absorbing boundary conditions for acoustic and elastic wave  
592 equations, *Bull. Seismol. Soc. Am.* **67**, 1529-1540.

593

594 Dixit, A. M., A. T. Ringler, D. F. Sumy, E. S. Cochran, S. E. Hough, S. S. Martin, S. Gibbons, J. H.  
595 Luetgert, J. Galetzka, S. N. Shrestha, et al. (2015). Strong-motion observations of the M 7.8 Gorkha,

596 Nepal, earthquake sequence and development of the N-SHAKE strong-motion network, *Seismol. Res.*  
597 *Lett.* **86**, 1533-1539.

598

599 Edwards, B., and D. Fäh (2013). Measurements of stress parameter and site attenuation from recordings  
600 of moderate to large earthquakes in Europe and the Middle East. *Geophys. J. Int.* **194**, 1190-1202.  
601

602 Esmailzadeh, A., D. Motazedian, and J. Hunter (2019). 3D nonlinear ground-motion simulation using a  
603 Physics-based method for the Kinburn basin, *Bull. Seismol. Soc. Am.* **109**, 1282-1311.  
604

605 Field, E. H., P. A. Johnson, I. A. Beresnev, and Y. Zeng (1997). Nonlinear ground-motion amplification  
606 by sediments during the 1994 Northridge earthquake, *Nature* **390**, 599-602.  
607

608 Field, E.H. (2000), A modified ground motion attenuation relationship for southern California the  
609 accounts for detailed site classification and a basin depth effect, *Bull. Seism. Soc. Am.* **90**, S209-S22.  
610

611 Frankel, A., W. Stephenson, and D. Carver (2009). Sedimentary basin effects in Seattle, Washington:  
612 Ground-motion observations and 3D simulations, *Bull. Seism. Soc. Am.* **99**, 1579-1611.  
613

614 Graves, R. W., and A. Pitarka (2004). Broadband time history simulation using a hybrid approach. 13<sup>th</sup>  
615 World Conference on Earthquake Engineering, Vancouver, B. C., Canada, Paper No. 1098.  
616

617 Harmsen, S., S. Hartzell, and P. Liu (2008). Simulated ground motion in Santa Clara Valley, California,  
618 and vicinity from  $M \geq 6.7$  scenario earthquakes, *Bull. Seism. Soc. Am.* **98**, 1243-1271.  
619

620 Harris, R. A., M. Barall, B. Aagaard, S. Ma, D. Roten, K. Olsen, B. Duan, D. Liu, B. Luo, K. Bai, et al.  
621 (2018). A suite of exercises for verifying dynamic earthquake rupture codes, *Seismol. Res. Lett.* **89**, 1146-  
622 1162.  
623

624 Hauksson, E., and P. M. Shearer (2006). Attenuation models (QP and QS) in three dimensions of the  
625 southern California crust: Inferred fluid saturation at seismogenic depths, *J. Geophys. Res. Solid*  
626 *Earth* **111**, B05302.  
627

628 Hough, S. E., E. Thompson, G. A. Parker, R. W. Graves, K. W. Hudnut, J. Patton, T. Dawson, T.  
629 Ladinsky, M. Oskin, K. Sirorattanakul, et al. (2020). Near-field ground motions from the July 2019  
630 Ridgecrest, California, earthquake sequence, *Seismol. Res. Lett.* **91**, 1542-1555.  
631

632 Huang, Y., J. P. Ampuero, and D. V. Helmberger (2014). Earthquake ruptures modulated by waves in  
633 damaged fault zones, *J. Geophys. Res. Solid Earth* **119**, 3133-3154.  
634

635 Ida, Y. (1972). Cohesive force across the tip of a longitudinal-shear crack and Griffith's specific surface  
636 energy, *J. Geophys. Res.* **77**, 3796-3805.  
637



638 Joyner, W. B., and D. M. Boore (1988). Measurement, characterization, and prediction of strong ground  
639 motion, In *Earthquake Engineering and Soil Dynamics II, Proc. Am. Soc. Civil Eng. Geotech. Eng. Div.*  
640 *Specialty Conf.* 27-30.

641

642 Kaklamanos, J., and B. A. Bradley (2018). Challenges in predicting seismic site response with 1D  
643 analyses: Conclusions from 114 KiK-net vertical seismometer arrays, *Bull. Seism. Soc. Am.* **108**, 2816-  
644 2838.

645

646 Kaklamanos, J., B. A. Bradley, A. N. Moolacattu, and B. M. Picard (2020). Physical hypotheses for  
647 adjusting coarse profiles and improving 1D site-response estimation assessed at 10 KiK-net sites, *Bull.*  
648 *Seism. Soc. Am.* **110**, 1338-1358.

649

650 Kubo, H., T. Nakamura, W. Suzuki, Y. P. Dhakal, T. Kimura, T. Kunugi, N. Takahashi, and S. Aoi  
651 (2019). Ground-Motion Characteristics and Nonlinear Soil Response Observed by DONET1 Seafloor  
652 Observation Network during the 2016 Southeast Off-Mie, Japan, *Bull. Seism. Soc. Am.* **109**, 976-986.

653

654 Ludwig, W. J. (1970). Seismic refraction, *The sea* **4**, 53-84.

655

656 Meza-Fajardo, K. C., J. F. Semblat, S. Chaillat, and L. Lenti (2016). Seismic-wave amplification in 3D  
657 alluvial basins: 3D/1D amplification ratios from fast multipole BEM simulations, *Bull. Seism. Soc.*  
658 *Am.* **106**, 1267-1281.

659

660 Moczo, P., J. Kristek, and L. Halada (2004). The finite-difference method for seismologists, *An*  
661 *Introduction. Comenius University, Bratislava.*

662

663 Neighbors, C., E. J. Liao, E. S. Cochran, G. J. Funning, A. I. Chung, J. F. Lawrence, C. Christensen, M.  
664 Miller, A. Belmonte, and H. H. A. Sepulveda (2015). Investigation of the high-frequency attenuation  
665 parameter,  $\kappa$  (kappa), from aftershocks of the 2010 M w 8.8 Maule, Chile earthquake, *Geophys. J.*  
666 *Int.* **200**, 200-215.

667

668 Olsen, K. B. (2000). Site amplification in the Los Angeles basin from three-dimensional modeling of  
669 ground motion, *Bull. Seism. Soc. Am.* **90**, S77-S94.

670

671 Park, S., and S. Elrick (1998). Predictions of shear-wave velocities in southern California using surface  
672 geology, *Bull. Seism. Soc. Am.* **88**, 677-685.

673

674 Pitarka, A., L. A. Dalguer, S. M. Day, P. G. Somerville, and K. Dan (2009). Numerical study of ground-  
675 motion differences between buried-rupturing and surface-rupturing earthquakes, *Bull. Seism. Soc. Am.* **99**,  
676 1521-1537.

677

678 Pitarka, A., R. Gok, G. Yetirmishli, S. Ismayilova, and R. Mellors (2016). Ground motion modeling in the  
679 eastern caucasus. *Pure Appl. Geophys.* **173**, 2791-2801.

680

681 Rodgers, A. J., A. Pitarka, N. A. Petersson, B. Sjögreen, and D. B. McCallen (2018). Broadband (0–4 Hz)  
682 ground motions for a magnitude 7.0 Hayward fault earthquake with three-dimensional structure and  
683 topography, *Geophys. Res. Lett.* **45**, 739-747.

684  
685 Rodgers, A. J., A. Pitarka, R. Pankajakshan, B. Sjögreen, and N. A. Petersson (2020). Regional-Scale 3D  
686 Ground-Motion Simulations of Mw 7 Earthquakes on the Hayward Fault, Northern California Resolving  
687 Frequencies 0–10 Hz and Including Site-Response Corrections, *Bull. Seism. Soc. Am* **110**, 2862-2881.

688  
689 Somerville, P. (2004). Differences in Earthquake Source and Strong Ground Motion Characteristics  
690 Between Shallow and Buried Faulting, In *Proceedings of OECD/NEA Workshop* (p. 5).

691  
692 Taborda, R., and J. Bielak (2014). Ground-motion simulation and validation of the 2008 Chino Hills,  
693 California, earthquake using different velocity models, *Bull. Seism. Soc. Am* **104**, 1876-1898.

694  
695 Trifunac, M. D., and M. I. Todorovska (1998). Nonlinear soil response as a natural passive isolation  
696 mechanism—the 1994 Northridge, California, earthquake, *Soil Dynam. Earthq. Eng.* **17(1)**, 41-51.

697  
698 Van Houtte, C., S. Drouet, and F. Cotton (2011). Analysis of the origins of  $\kappa$  (kappa) to compute hard  
699 rock to rock adjustment factors for GMPEs, *Bull. Seism. Soc. Am* **101**, 2926-2941.

700  
701 Wang, Y., S. M. Day, and M. A. Denolle (2019). Geometric controls on pulse-like rupture in a dynamic  
702 model of the 2015 Gorkha earthquake, *J. Geophys. Res. Solid Earth* **124**, 1544-1568.

703  
704 Wang, Y. J., K. F. Ma, S. K. Wu, H. J. Hsu, and W. C. Hsiao (2016). Near-Surface Attenuation and  
705 Velocity Structures in Taiwan from Wellhead and Borehole Recordings Comparisons, *TAO* **27**, 169-180.

706  
707 Wills, C., M. Petersen, W. Bryant, M. Reichle, G. Saucedo, S. Tan, G. Taylor, and J. Treiman (2000), A  
708 site-condition map for California based on geology and shear-wave velocity, *Bull. Seism. Soc. Am.* **90**,  
709 S187-S208.

710  
711 Withers, K. B., K. B. Olsen, and S. M. Day (2015). Memory-efficient simulation of frequency-dependent  
712 Q, *Bull. Seism. Soc. Am.* **105**, 3129-3142.

713  
714 Withers, K. B., K. B. Olsen, S. M. Day, and Z. Shi (2019). Ground Motion and Intraevent Variability  
715 from 3D Deterministic Broadband (0–7.5 Hz) Simulations along a Nonplanar Strike-Slip Fault Ground  
716 Motion and Intraevent Variability from 3D Deterministic Broadband Simulations, *Bull. Seism. Soc.*  
717 *Am.* **109**, 229-250.

718  
719  
720 **Full mailing address for each author**

721  
722 Room 4534F, 1100 North University, Ann Arbor, MI 48109

723  
724  
725

726 **List of Figure Captions**

727

728 Figure 1. Depth variations of (a) material properties, (b) frictional parameters, and (c) fault  
729 stresses in model S. Model R uses the same fault friction and stresses as shown in (b) and (c).

730 Figure 2. Comparison of (a and b) spatiotemporal distribution of slip rate, (c) slip and (d) slip  
731 rate (low-pass filtered at 4 Hz) for model S and model R. (c) and (d) show results at depths of 1,  
732 2, 3 and 4 km from left to right.

733 Figure 3. Plots of (a-d) simulated acceleration waveforms and (e) spectra for soil and rock sites  
734 at a distance of 10 km from the fault for surface rupture. The dotted and dash-dot lines show  
735 acceleration spectra for elastic soil and rock simulations.

736 Figure 4. Plots of (a-c) simulated HVSRs and (d-f) normalized HVSRs for soil and rock sites at  
737 distances of (a and d) 5, (b and e) 10 and (c and f) 15 km from the fault for surface rupture. The  
738 dashed lines show results from a rock simulation with different attenuation parameters from the  
739 soil simulation, whereas the dash-dot lines show results from a rock simulation with the same  
740 attenuation parameters as soil.

741 Figure 5. Illustrations of (a) the depth variation of seismic wave velocities for the 16-layer  
742 velocity model (solid lines) and the 5-layer velocity model (dashed lines) compared to the  
743 smooth velocity gradient (dotted and dash-dot lines), as well as (b-g) simulated HVSRs for soil  
744 and rock sites at distances of (b and e) 5, (c and f) 10 and (d and g) 15 km from the fault for the  
745 16-layer and 5-layer velocity models (solid and dashed lines) compared to the simulated HVSRs  
746 for soil and rock sites in smooth velocity models (dotted lines).

747 Figure 6. Plots of (a-d) simulated acceleration waveforms and (e) spectra for soil and rock sites  
748 at a distance of 10 km from the fault for buried rupture.

749 Figure 7. Plots of (a-c) simulated HVSRs and (d-f) normalized HVSRs for soil and rock sites at  
750 distances of (a and d) 5, (b and e) 10 and (c and f) 15 km from the fault for buried rupture.

751 Figure 8. Plots of (a-c) simulated HVSRs and (d-f) normalized HVSRs for soil and rock sites at  
752 distances of (a and d) 5, (b and e) 10 and (c and f) 15 km from the fault for a double-couple  
753 source.

754 Figure 9. Illustrations of (a) the variation of  $V_p$  (solid line),  $V_s$  (dashed line) and density (dash-  
755 dotted line) in the new soil velocity model for the top 100 m compared to the previous soil  
756 velocity model (dotted lines), as well as (b-d) simulated HVSRs and (e-g) normalized HVSRs for  
757 soil and rock sites at distances of (b and e) 5, (c and f) 10 and (d and g) 15 km from the fault.